Supporting Information

Switching of Electron and Ion Conductions by Reversible H_2O Sorption in n-Type Organic Semiconductor

Haruka Abe,[1] Ayumi Kawasaki,[1] Takashi Takeda,[1, 2] Norihisa Hoshino,[1, 2] Wakana Matsuda,[3] Shu Seki,[3*] Tomoyuki Akutagawa[1, 2*]

E-mail: akutagawa@tohoku.ac.jp and seki@moleng.kyoto-u.ac.jp

Contents

9. The n−dependent transient conductivities of $(K^+)_2$•**PCNDI**$^{2-}$•n(H_2O) based on the FP-TRMA spectra (Figure S8).
10. TAS profile of $(K^+)_2$**PCNDI**$^{2-}$•n(H_2O) (Figure S9).
11. The *T*- and *f*-dependent dependent imaginary part dielectric constants ε_2 of crystals $(K^+)_2$**PCNDI**$^{2-}$•n(H_2O) (Figure S10).
12. DSC diagram of the unhydrated crystals $(K^+)_2$**PCNDI**$^{2-}$ (Figure S11).
13. The n-dependent K^+ conductivity (σ_{ion}) and activation energy (E_a) (Figure S12).

Experimental Section

General. Ultraviolet/visible/near infrared (UV–vis–NIR) spectra (200–3000 nm) and infrared (IR) spectra (400–4000 cm^{-1}) were obtained for the samples in solution and on KBr pellets and were measured using PerkinElmer Lambda 750 and Thermo Fisher Scientific Nicolet 6700 FT-IR spectrophotometers, respectively. Redox potentials were measured for 0.1 mM solutions of the samples dissolved in H_2O. 0.1 M *n*-Bu_4N•Br was used as the supporting electrolyte; platinum wire was used as the working and counter electrodes; and Ag/AgCl was used as the reference electrode. The redox potentials were scanned at 50 mV s^{-1} and were calibrated using the half-wave oxidation potential of Fc/Fc^+ (0.554 V). Thermogravimetric (TG) and differential thermal (DT) analyses were performed using a Rigaku Thermo Plus TG8120 thermal analysis station and an Al_2O_3 reference. The samples were heated in the range 293–600 K at 5 K min^{-1} under nitrogen. Temperature-dependent dielectric constants were measured using the two-probe AC impedance method over a frequency range from 10^2 to 1000×10^3 Hz (HP4194A). The single crystal was placed in a heating stage of Linkam LTS350 and the measurement axis was determined by the single crystal X-ray structural analysis. The electrical contacts were prepared using gold paste to attach the 10 μm ϕ gold wires.

Preparation of H2PCNDI.[S1] Commercially available *β*-alanine (3.56 g, 40.0 mmol) and 1,4,5,8-naphtalene dicarboxylic acid dihydrate (5.37 g, 20.0 mmol) were dissolved in DMF (40 mL) and were refluxed at 90 °C overnight under ambient condition The reaction mixture was cooled to room temperature, and was collected by the filtration and dried under vacuum. The resultant powder was washed by DMF and EtOH to obtain a yellow powder (7.80 g) with a yield of 95%. Anal. Calc. for $C_{20}H_{14}N_2O_8$: C 58.54, H 3.44, N 6.83; Found C 58.04, H 3.64, N 7.03. ^{1}HNMR (400 MHz, DMSO-d_6) : δ 12.41 (s, 2H, COOH); 8.68 (s, 4H, Ar-H); 4.28 (t, 4H, J = 7.7 Hz, -N-CH_2); 2.64 (t, 4H, J = 7.8 Hz, -CH_2-).

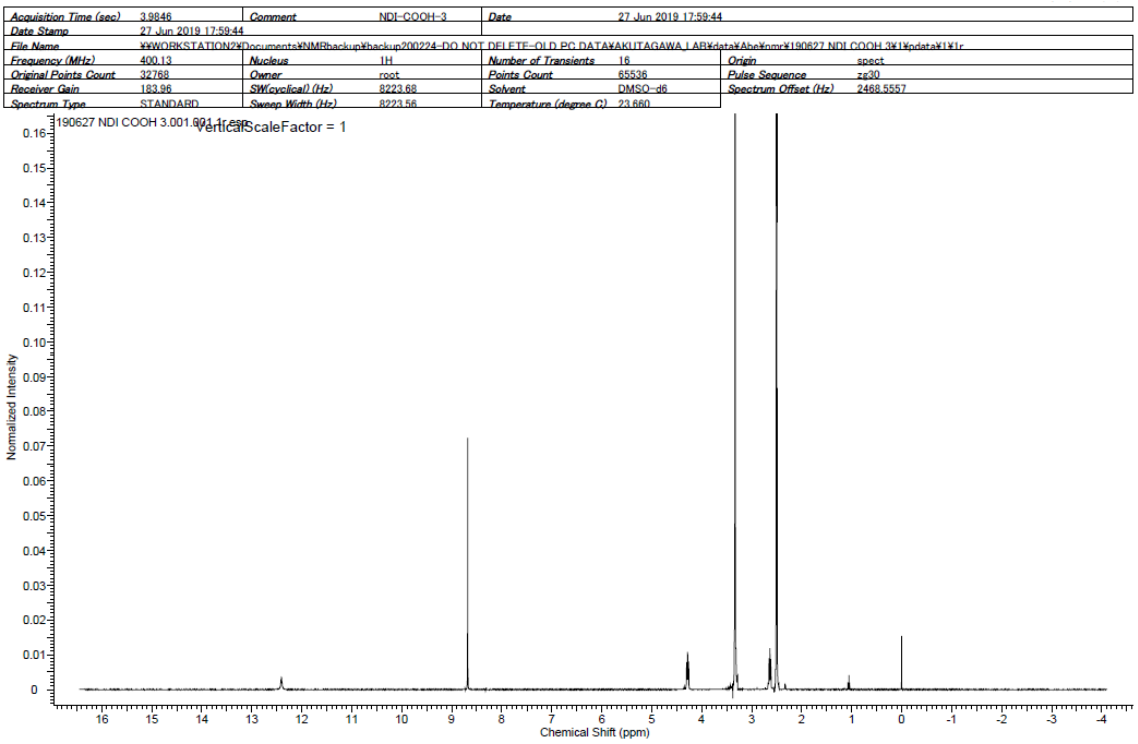

Figure S0. ^{1}H NMR spectra of **H2PCNDI** in DMOS-d_6.

Preparation of $(K^+)_2$PCNDI^{2-}•n(H_2O). Aqueous KOH solution (0.115 M, 0.786 g KOH was solved in 122 mL H_2O) and H2PCNDI (2.45 g, 6.09 mmol) were mixed and refluxed at 100 °C during 4 fours. The solvent H_2O was removed in vacuum, and the resultant powder was recrystallized by H2O (21 mL) - EtOH (27 mL), and was collected by the filtration and dried under vacuum. Yellow powder (633 mg) of $(K^+)_2$**PCNDI^{2-}**•0.5(H_2O) was obtained as a yield of 21%. Anal. Calc. for $C_{20}H_{13}N_2O_{8.5}K_2$: C 48.48, H 2.64, N 5.65; Found C 48.49, H 2.79, N 5.61.

The unhydrated crystals $(K^+)_2$**PCNDI^{2-}** were obtained by thermal treatment at 400 K under N_2 flow or in vacuum. The thin film of $(K^+)_2$ **PCNDI^{2-}**•4(H_2O) was prepared by a drop-cast method on quartz substrate, which was dried under the ambient condition.

Crystal structural analysis. Single crystals were obtained by slowly evaporating the crystallisation solvents. Crystallographic data were collected using a Rigaku RAPID-II diffractometer equipped with a rotating anode fitted with a multilayer confocal optic and using Cu-Kα (λ = 1.54187 Å) radiation from a graphite monochromator. Structural refinements were performed using the full-matrix least-squares method on F^2. Calculations were performed using Crystal Structure

software packages.[S2, S3] All the parameters, except for those of the hydrogen atoms, were refined using anisotropic temperature factors. Crystal data of $(K^+)_2$**PCNDI**$^{2-}$•4(H_2O), $C_{20}H_{20}N_2O_{12}K_2$, F.W. = 558.58: crystal dimensions, 0.30 x 0.20 x 0.01 mm^3, T = 100K, μ = 43.762 cm^{-1}, Monoclinic $P2_1/c$ (#14), Z = 2, a = 16.271(2), b = 8.4478(10), c = 8.1981(10) Å, β = 91.212(4), V = 1126.6(2) Å^3, 12205 collected, 2043 unique, R_{init} = 0.1572, R_1= 0.0939, R_{all} = 0.1716, R_w = 0.3015. G.O.F = 0.820. The maximum and minimum peaks on the final difference Fourier map corresponded to 0.34 and -0.57e$^-$ Å^{-3}, respectively.

Flash-photolysis time-resolved microwave conductivity measurements. Thin films of crystals $(K^+)_2$•**PCNDI**$^{2-}$•n(H_2O) were fabricated by drop-casting their aqueous solutions onto quartz substrates (9 × 40 mm^2 × 1 mm thick), which were then dried under vacuum (< 2 × 10^{-1} Pa) for 1 h to remove any residual water and subsequently annealed at 120 °C. Charge carrier mobilities were evaluated by flash-photolysis time-resolved microwave conductivity (FP-TRMC) under Ar-saturation conditions at 290 K.[39, 40] Charge carriers were injected into the materials via photoionisation with third-harmonic-generating (λ = 355 nm) Nd:YAG laser (Spectra Physics model INDI-HG) pulses at 10 Hz at ca. 5 ns pulse^{-1}. The photon density of a 355 nm pulse was modulated in the rage 4.8–6.1 × 10^{15} photons cm^{-2} pulse^{-1}. The microwave frequency and power were set at ~9.1 GHz and 3 mW, respectively, and were guided into a microwave cavity. The Q-factors of the microwave cavity loaded with the samples were 1900 and 2200 at 470 and 290 K, respectively, and the film-coated substrates were set at the maximum electric field. The reflected power of the probing microwave, picked up by a diode (rise time < 1 ns), was amplified by a Ciao Electronics CA812-304 FET amplifier and was subsequently monitored by a Tektronix model TDS3032B digital oscilloscope. The observed change in the reflected microwave power (ΔP_r) was normalised with the steady reflection of the microwave from the cavity (P_r) and was directly converted into the product of a photocarrier generation yield (ϕ) and the sum of photogenerated electron/hole mobilities ($\Sigma\mu$):

$$\phi\Sigma\mu = 1/(eI_0F_{light}) \times (1/A) \times (\Delta P_r/P_r), \quad (1)$$

where ε, A, I_0, and F_{light} are elementary charge, sensitivity factor (S^{-1} cm), incident photon density of the excitation laser (photons cm^{-2}), and filling factor (cm^{-1}), respectively. F_{light} was calculated based on the overlap between the photocarrier injection area (presumed to be proportional to the excitation light absorbed by the sample film) and the electric field strength distribution in the cavity, as derived from a calculation code of CST Microwave Studio (AET Inc.).

Transient absorption spectroscopy measurements. To determine the values of ϕ, transient absorption spectroscopy (TAS) was conducted at 290 K for polycrystalline films of crystals **1** and **2** drop-cast onto quartz substrates identical to those used for the FP-TRMC measurements. The optical transmittances of the films were measured for various excitation light pulses, using an Ophir VEGA power meter equipped with a PE25-C sensor head (Newport Corp.) Changes in the time-dependent absorption spectra were measured as two-dimensional images by a Hamamatsu C7700 streak camera via a Hamamatsu C5094 spectrometer upon direct excitation of the films by pulses from the laser system identical to the one used for the FP-TRMC measurements. The excitation density was tuned at 3.2×10^{16} cm^{-2} photons $pulse^{-1}$. The streak images were averaged typically over 400 scans to correct 2D time–wavelength correlation data of the transient absorption of each film.

Theoretical calculations. The LUMOs of molecules **PCNDI^{2-}** were calculated with density functional theory (DFT) using the B3LYP/6-31+G(d, p) basis set (Gaussian 09).[S4] Atomic coordinates based on the X-ray structural analyses were used for single-point energy calculations. The transfer integrals (t) between the LUMOs of **H2PCNDI** were calculated within the tight-binding approximation, using the extended Hückel molecular orbital method, where the LUMOs of protonated **H2BSNDI** were used as the basis functions.[S5] Semi-empirical parameters for Slater-type atomic orbitals were obtained from the literature.[S5] The t values for each pair of molecules were assumed to be proportional to the overlap integral (S) according to the equation $t = -10S$ (eV).

References

S1) Zhang, L.; Zhang, Z.; He, C.; Dai, JL.; Liu, J.; Wang, L.; Rationally Designed Surfactants for Few-Layered Graphene Exfoliation: Ionic Groups Attached to Electron-Deficient p-Conjugated Unit through Alkyl Spacers, *ACS Nano*, **2014**, *7*, 6663-6670.

S2) Crystal Structure: Single crystal structure analysis software. Ver. 3.6, 2004. Rigaku Corporation and Molecular Structure Corporation.

S3) Sheldrick, G. M. SHELX97 Programs for Crystal Structure Analysis; Universitat Göttingen: Göttingen, Germany, 1998.

S4) Gaussian 09, Revision C 01: Frisch, M. J.; Trucks, G. W.; Schlegel, H. B.; Scuseria, G. E.; Robb, M. A.; Cheeseman, J. R.; Scalmani, G.; Barone, V.; Mennucci, B.; Petersson, G. A.; et al Gaussian, Inc.: Wallingford, CT, 2009.

S5) Mori, T.; Kobayashi, A.; Sasaki, Y.; Kobayashi, H.; Saito, G.; Inokuchi, H. *Bull. Chem. Soc. Jpn*. **1984**, *57*, 627–633.

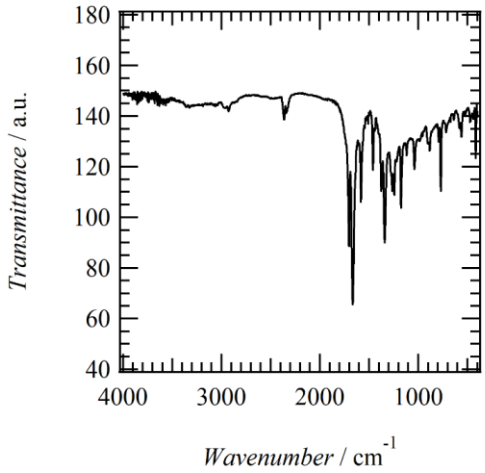

Figure S1. The IR spectra of $(K^+)_2$**PCNDI**$^{2-}$•n(H_2O) on KBr pellet.

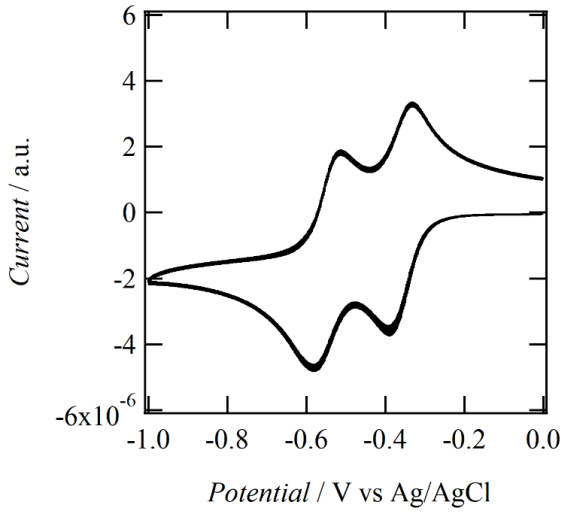

Figure S2. The two-steps reversible half-wave reduction potentials ($E^1_{1/2}$ and $E^2_{1/2}$) of **PCNDI**$^{2-}$ vs. Ag/AgCl reference electrode in H_2O.

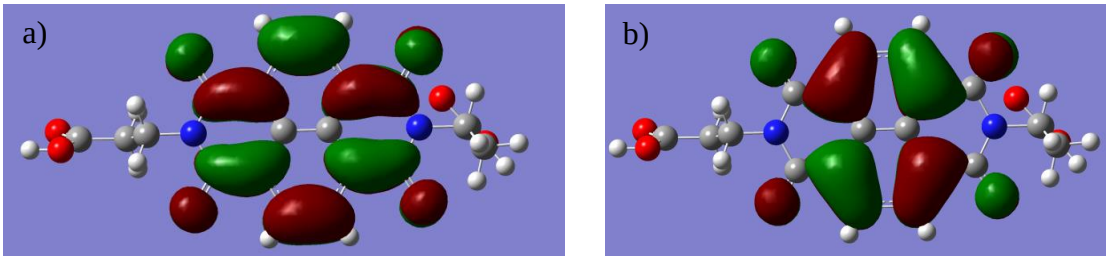

LUMO -0.14058 a.u.
= -3.8254 eV

HOMO -0.27134 a.u.
= -7.3836 eV

Figure S3. The lowest occupied molecular orbitals (LUMOs) and the highest occupied molecular orbitals (HOMOs) of a) **H2PCNDI** and b) *N*,*N*'-diphenyl-**NDI** calculated with density functional theory (DFT) using the B3LYP/6-31+G(*d*, *p*) basis set (Gaussian 09).

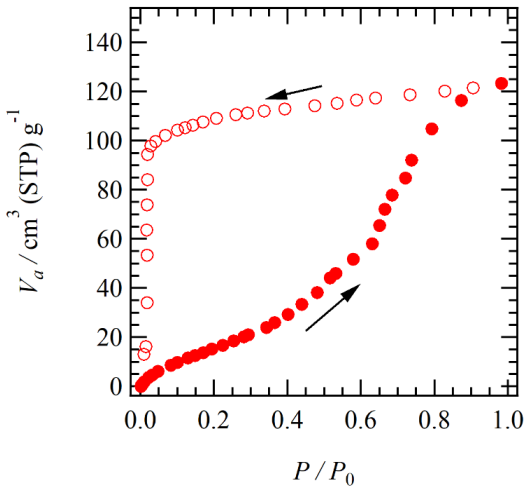

Figure S4. The P/P_0 – $\underline{V}_a$ plots of H_2O adsorption – desorption isotherm of $(K^+)_2$•**PCNDI**$^{2-}$ at 298K.

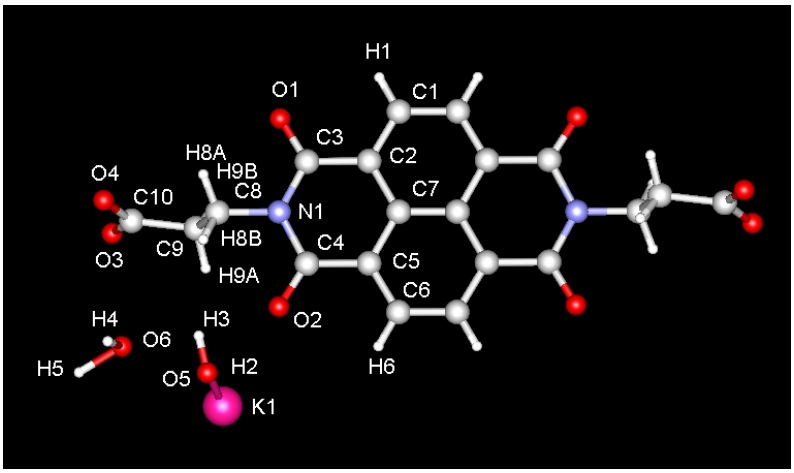

Figure S5. Atomic numbering scheme of crystallographicaly independent half unit of $(K^+)_2$**PCNDI**$^{2-}$•4(H_2O) based on the single crystal X-ray structural analysis at 100K.

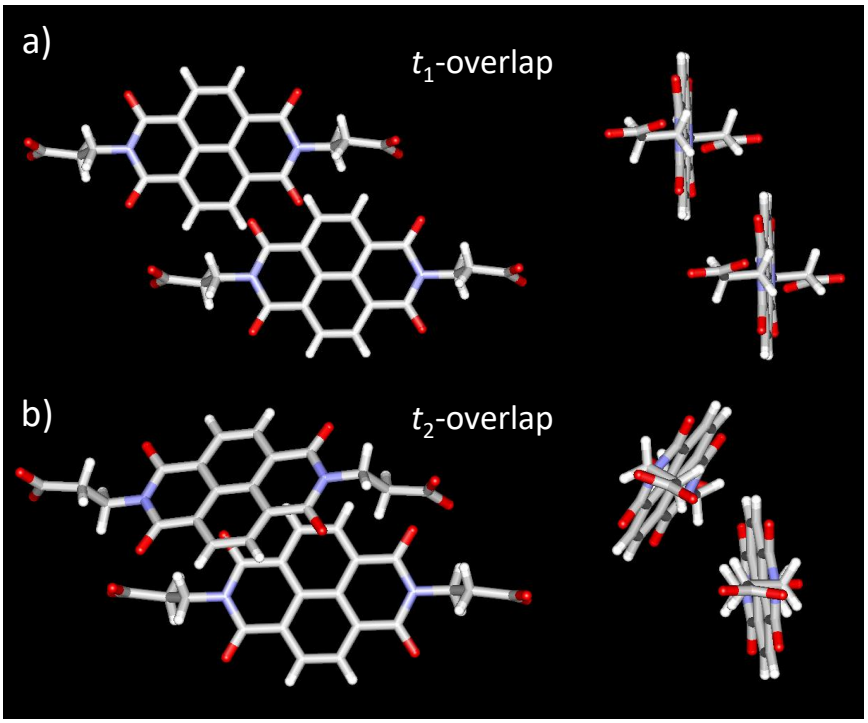

Figure S6. Two kinds of π-stacking mode of t_1 and t_2 in crystal $(K^+)_2$**PCNDI**$^{2-}$•4(H_2O).

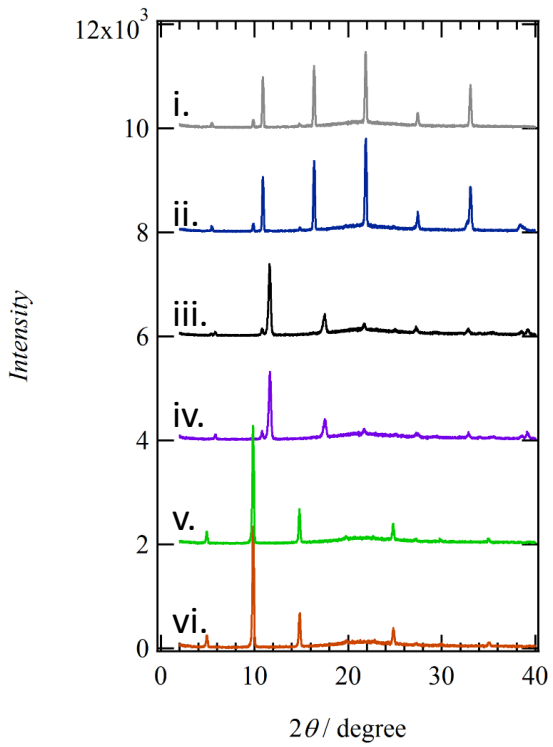

Figure S7. The PXRD patterns of crystals $(K^+)_2$**PCNDI**$^{2-}$•n(H_2O). i) Under ambient condition at 298K, ii) after 5 min dry N_2 flow (500 mL min^{-1}) at 298K, iii) heating at 400K under dry N_2 flow, iv) cooling down to 298 K under dry N_2 flow, v) 20 min H_2O saturated N_2 flow at 298K, and vi) 5 min dry N_2 flow at 298K.

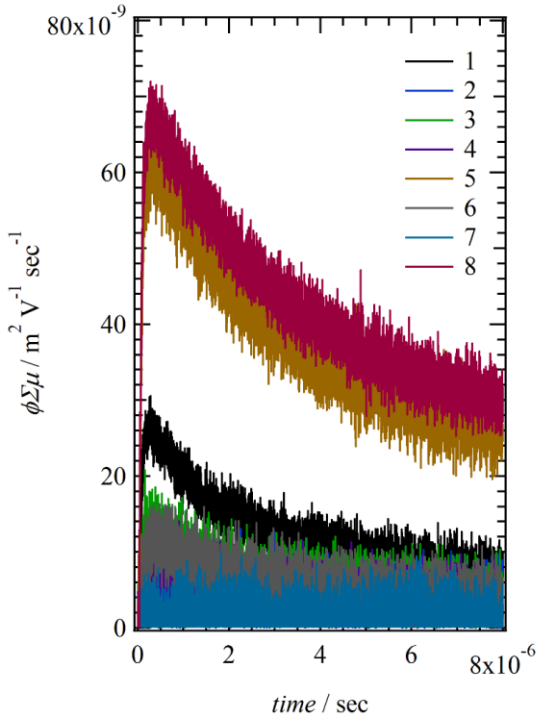

Figure S8. The n−dependent transient conductivities of $(K^+)_2$•**PCNDI^{2-}**•n(H_2O). FP-TRMA spectra of i) ambient condition at 298K, ii) dry N_2 flow at 298K, iii) dry N_2 flow at 291K, iv) dry N_2 flow at 298K after the heating up to 400K, v) ambient condition after the exposure to H_2O saturated N_2 flow at 298K, vi) 5 min dry N_2 flow at 298K, vii) dry N_2 flow at 298 K after the heating up to 400K, and viii) ambient condition at 298K after 20 min exposure to H_2O saturated N_2 flow.

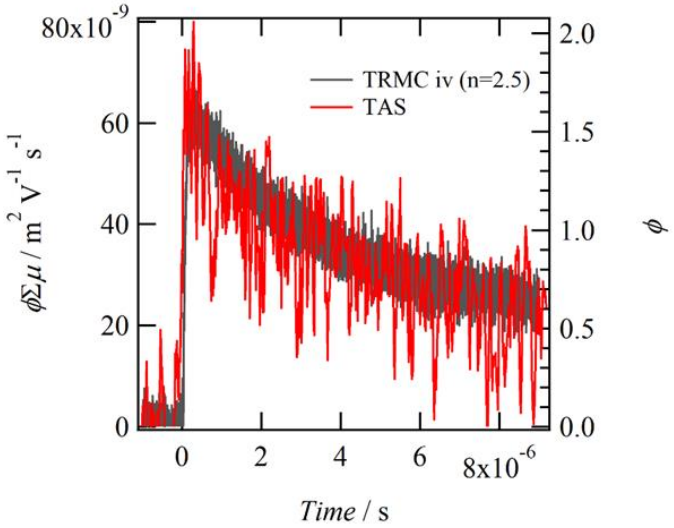

Figure S9. TAS profile of $(K^+)_2$**PCNDI**$^{2-}$•n(H_2O).

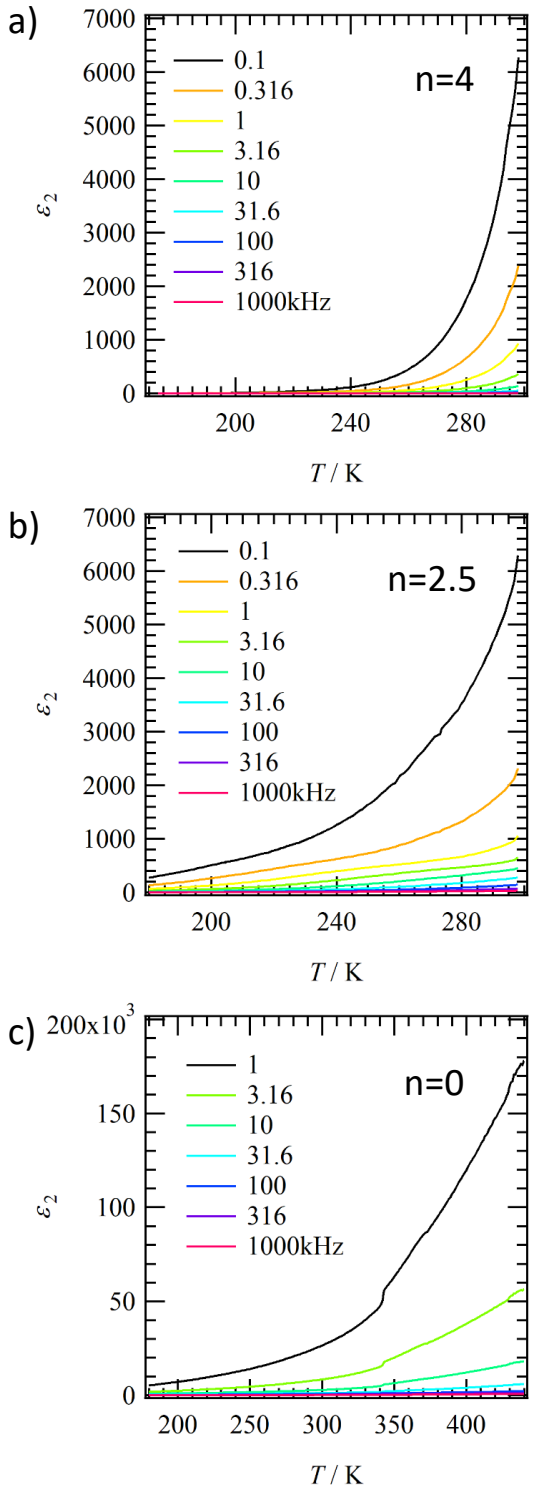

Figure S10. The *T*- and *f*-dependent dependent imaginary part dielectric constants ε_2 of crystals $(K^+)_2$**PCNDI**$^{2-}$•n(H_2O) with a) n=4.0, b) n=2.5, and c) n=0 on compressed pellets.

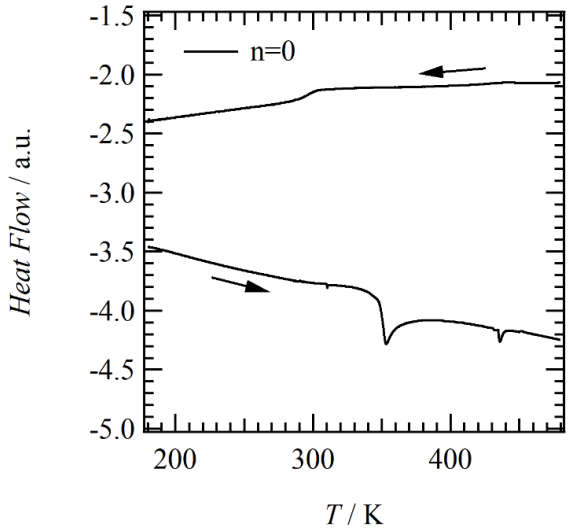

Figure S11. DSC diagram of the unhydrated crystals $(K^+)_2$**PCNDI**$^{2-}$. In the temperature range from 180 to 480K. A phase transition behaviour was observed around 350K in the heating process.

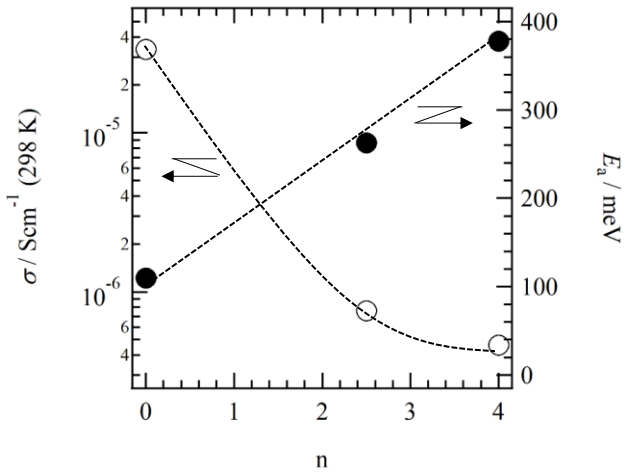

Figure S12. The n-dependent K^+ conductivity (σ_{ion}) and activation energy (E_a).